Trace Elements in Magnetite from the Pagoni Rachi Porphyry Prospect, NE Greece: Implications for Ore Genesis and Exploration

Constantinos Mavrogonatos [1,*] **, Panagiotis Voudouris** [1] **, Jasper Berndt** [2] **, Stephan Klemme** [2] **,**
Federica Zaccarini [3] **, Paul G. Spry** [4] **, Vasilios Melfos** [5] **, Alexandre Tarantola** [6] **,**
Manuel Keith [7] **, Reiner Klemd** [7] **and Karsten Haase** [7]

[1] Faculty of Geology and Geoenvironment, National and Kapodistrian University of Athens, 15784 Athens, Greece; voudouris@geol.uoa.gr
[2] Institut für Mineralogie, Westfälische-Wilhelms Universität Münster, 48149 Münster, Germany; jberndt@uni-muenster.de (J.B.); stephan.klemme@uni-muenster.de (S.K.)
[3] Department of Applied Geosciences and Geophysics, University of Leoben, 8700 Leoben, Austria; federica.zaccarini@unileoben.ac.at
[4] Department of Geological and Atmospheric Sciences, Iowa State University, Ames, IA 50011-1027, USA; pgspry@iastate.edu
[5] Faculty of Geology, Aristotle University of Thessaloniki, 54124 Thessaloniki, Greece; melfosv@geo.auth.gr
[6] UMR GeoResources, Faculté des Sciences et Technologies, Université de Lorraine, 54506 Vandoeuvre-lès-Nancy, France; alexandre.tarantola@univ-lorraine.fr
[7] GeoZentrum Nordbayern, Universität Erlangen-Nürnberg, D-91054 Erlangen, Germany; Manuel.Keith@fau.de (M.K.); reiner.klemd@fau.de (R.K.); karsten.haase@fau.de (K.H.)
* Correspondence: kmavrogon@geol.uoa.gr; Tel.: +30-210-727-4794

Abstract: Magnetite is a common accessory phase in various types of ore deposits. Its trace element content has proven to have critical implications regarding petrogenesis and as guides in the exploration for ore deposits in general. In this study we use LA-ICP-MS (laser ablation-inductively coupled plasma-mass spectrometry) analyses of trace elements to chemically characterize magnetite from the Pagoni Rachi Cu–Mo–Re–Au porphyry-style prospect, Thrace, northern Greece. Igneous magnetite mostly occurs as euhedral grains, which are commonly replaced by hematite in fresh to propylitic-altered granodiorite porphyry, whereas, hydrothermal magnetite forms narrow veinlets or is disseminated in sodic/potassic-calcic altered (albite + K-feldspar + actinolite + biotite + chlorite) granodiorite porphyry. Magnetite is commonly associated with chalcopyrite and pyrite and locally exhibits martitization. Laser ablation ICP-MS analyses of hydrothermal magnetite yielded elevated concentrations in several trace elements (e.g., V, Pb, W, Mo, Ta, Zn, Cu, and Nb) whereas Ti, Cr, Ni, and Sn display higher concentration in its magmatic counterpart. A noteworthy enrichment in Mo, Pb, and Zn is an unusual feature of hydrothermal magnetite from Pagoni Rachi. High Si, Al, and Ca values in a few analyses of hydrothermal magnetite imply the presence of submicroscopic or nano-inclusions (e.g., chlorite, and titanite). The trace element patterns of the hydrothermal magnetite and especially the decrease in its Ti content reflect an evolution from the magmatic towards the hydrothermal conditions under decreasing temperatures, which is consistent with findings from analogous porphyry-style deposits elsewhere.

Keywords: magnetite; magmatic; hydrothermal; trace elements; LA-ICP-MS; porphyry; exploration

1. Introduction

Magnetite (Fe_3O_4), a mineral of the spinel group, is a common constituent in a wide variety of rock types and ore deposits. It forms under very different physicochemical conditions, which may extend from crystallization of silicate and sulfide melts at high magmatic temperatures, up to precipitation from hydrothermal fluids in low temperature environments [1]. Its chemistry is a function of various factors like sulfur and oxygen fugacity (fS_2, fO_2), temperature, cooling rate, silica activity, and melt/fluid composition (e.g., [1–5]). The sensitivity of magnetite to these parameters, results in variable concentrations of minor and trace elements including, Al, Ti, Mg, Mn, Zn, Cr, V, Ni, Co, and Ga [6].

Analytical methods such as laser ablation-inductively coupled plasma-mass spectrometry (LA-ICP-MS), allow us to analyze a wide range of trace elements in magnetite at very low detection limits (e.g., [7–9]). As magnetite is commonly found in many rocks and ore deposits, its trace elements content is of particular interest to geoscientists. Many studies revealed that certain enrichments and/or depletions in minor and trace elements reflect different mineralization styles and host rocks [5,7,10–16] This fact favors the use of magnetite chemistry both as a promising petrogenetic indicator and as an exploration tool.

Statistical interpretation of the trace element geochemistry of magnetite from different styles of mineralization, coupled with petrographic interpretations and elemental ratios, allowed the establishment of discriminant diagrams: Dupuis and Beaudoin [7] were among the first who correlated the composition of magnetite to its origin and formation conditions (e.g., magmatic vs. hydrothermal) and to different major deposit types (e.g., iron oxide copper-gold vs. porphyry deposits). They used the plots of Ca + Al + Mn versus Ti + V and of Ti + V versus Ni/(Cr + Mn), to distinguish the average composition of magnetite from iron oxide copper-gold (IOCG), Kiruna type iron oxide-apatite (IOA), skarn, banded iron formation (BIF), porphyry-Cu, Fe–Ti–V, and Ni–Cu–PGE deposits. These diagrams proved to be potentially useful in identifying magnetite of unknown origin, however it must be noted that magnetite can display a broad compositional variation, within a single deposit. In this context, Dare et al. [1] used the Ti, Ni, and Cr concentration of magnetite as a means to distinguish between hydrothermal and magmatic magnetite. By studying the composition of magnetite in porphyry-Cu and skarn deposits in the SW United States, Nadoll et al. [13,14] suggested that the compositional boundary between the two types of deposits is highly transitional. More recently, Canil et al. [15] used principal component analysis to suggest that the composition of magnetite from porphyry Cu–Au–Mo deposits in British Columbia is a function of temperature, oxygen fugacity, and nature/composition of the hydrothermal fluids. Based on detailed textural characterization and high-resolution in situ compositional analyses, Wen et al. [17] proposed that a V/Ti versus Fe diagram should be used to discriminate between pristine igneous magnetite, re-equilibrated magnetite, and hydrothermal magnetite. Finally, Pisiak et al. [18], via the use of linear discriminant analysis, calculated discriminant factors based on the composition of magnetite in barren and ore-related igneous rocks as well as hydrothermal magnetite, suggesting that the method was a useful tool when exploring for ore-related, magnetite-bearing intrusions.

Porphyry-type deposits, are not generally exposed at the surface and so, one aspect of exploring for such deposits has used potential indicator minerals such as apatite, epidote, garnet, and tourmaline as a guide (e.g., [19–22]). However, the chemical composition of igneous and hydrothermal magnetite and its association with the porphyry deposit subtypes and the magmatic affinity of the host intrusive rocks remains poorly constrained. Recently Huang et al. [16] have tried to establish the potential relationships among the composition of magnetite, the geochemical signature of the host rock, and the porphyry deposit sub-types.

Magnetite, despite being common in numerous geological environments in Greece, has been poorly studied to date. In this study, we make the first attempt to evaluate the composition of magmatic and hydrothermal magnetite from a porphyry-style mineralization, namely the Pagoni Rachi Cu–Mo–Re–Au prospect in north-eastern Greece. The trace element composition of magnetite was

used to monitor the physicochemical conditions of ore formation and to identify possible relations between the magnetite chemistry and the geochemical affinities of the host rock. Finally, we try to identify possible chemical fingerprints in the hydrothermal magnetite that could point towards ore-grade mineralized zones, in an attempt to establish a new exploration tool for porphyry-style deposits and prospects in Greece, and elsewhere.

2. Geological Setting

The Hellenides, comprise an elongated (more than 500 km long) mountain belt in Greece, which corresponds to a segment of the Alpine-Himalayan orogenic chain (e.g., [23]). They resulted from the still ongoing collision between the African and Eurasian plates, which began in the Late Jurassic, above the N-dipping Hellenic trench [24]. This collision produced a pile of SW-vergent thrusted nappes comprising three continental blocks (namely Rhodope, Adria, and Pelagonia) and their spatially related oceanic domains (now represented by the Vardar and Pindos ophiolitic suites) [25–29].

Lithologies of the Rhodope Massif (Figure 1 [30,31]) record a long and rather complex tectonometamorphic history [32]. Recent studies by Kydonakis et al. [28,29] of the tectonometamorphic evolution of the Rhodope Massif suggested that it comprises three major lithological units/sub-domains: (a) the Northern Rhodope Domain; (b) the Southern Rhodope Core Complex including the Kerdylion unit of the former Serbo-Macedonian Massif, and (c) the Chalkidiki Block, adjacent to the Serbo-Macedonian Massif, but excluding the Kerdylion unit.
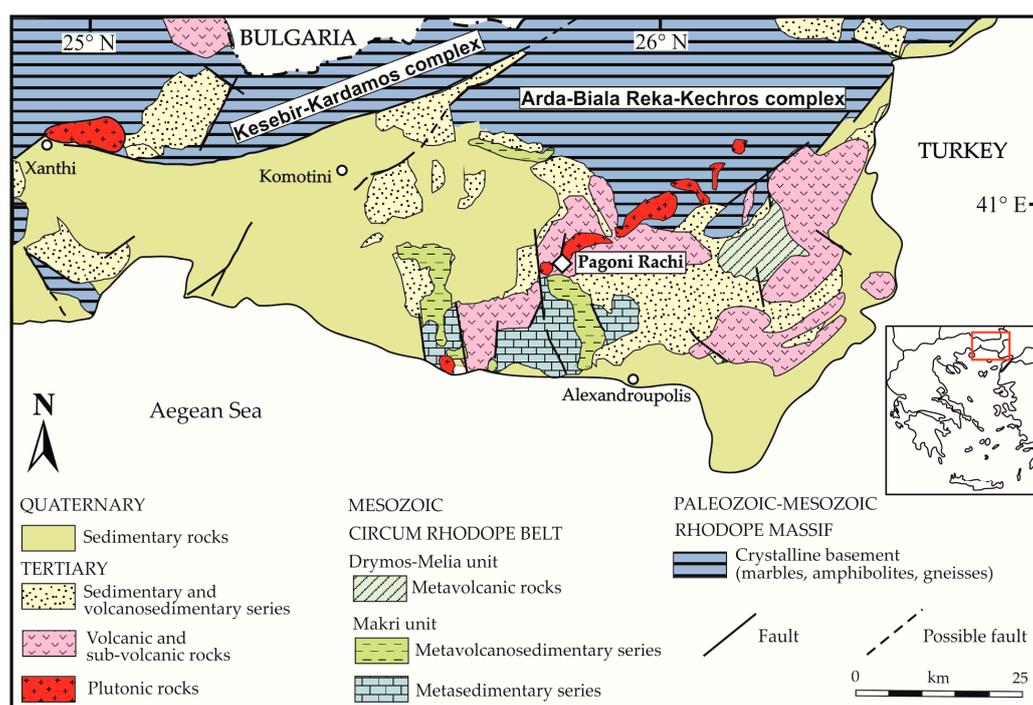
Figure 1. Geological map of NE Greece (after Voudouris et al., [30]; Mavrogonatos et al., [31]). The white diamond marks the location of the study area.

The Northern Rhodope Domain, which occupies most of the NE part of Greece (Figure 1), consists of (a) a structurally lower high-grade gneissic basement derived from Permo-Carboniferous protoliths, subdivided into the Arda, Biala Reka-Kechros, and Kesebir-Kardamos migmatitic domes; (b) an intermediate unit of high-metamorphic grade basement rocks, whose protoliths yield two age intervals (Neoproterozoic to Ordovician and Permo-Carboniferous to Early Cretaceous); and (c) a structurally upper and low metamorphic grade unit known as Circum-Rhodope Belt, including several sub-units (e.g., Drymos-Melia, Makri) as well as the Evros ophiolite [33–35].

Exhumation of the deep-seated lithologies in the Rhodope Massif took place at 40–35 Ma [26,35,36] and the second, at ~35 Ma [35]. Activation of major detachment faults resulted in the exhumation of deep lithologies, thus forming the metamorphic core complexes, and in the opening of several E-W trending, structurally-controlled basins [25,37]. Syn-extensional sedimentation resulted in the formation of thick clastic rock sequences (transgressive conglomerates, sandstones/claystones and limestones). Contemporaneous asthenospheric upwelling triggered by crustal thinning, generated magmatic rocks of Eocene to Miocene age, with a pronounced post-subduction signature [38–40]. These magmatic rocks are characterized by calc-alkaline to shoshonitic and ultra-potassic affinities, and display a mafic to felsic compositional range [38,41–43].

Subsequent hydrothermal alteration of the magmatic and/or the sedimentary rocks led to the formation of significant metallic mineralization, mainly in the Rhodope (Thrace), and to a lesser extent the Serbo-Macedonian (Chalkidiki) domains [39,42,44,45].

The metallogenic province of Thrace hosts a plethora of porphyry- and epithermal-style deposits and prospects (see Melfos and Voudouris [44]; Voudouris et al. [45]), which are enriched in a variety of elements, including precious and critical metals (e.g., Au, Ag, Re, Te, Se, In, Ga, and Ge). A number of porphyry style deposits has been recognized in the broader area with the most important of them being the Konos Hill [31,46–49], the Pagoni Rachi [50–52], and the Maronia [53] Cu–Mo–Re–Au systems, as well as the recently discovered porphyry Mo prospect in the Aisymi-Leptokarya area [45,54]. Epithermal-style mineralization in the area include, among others, the important Viper [55] and Perama Hill [56] Au–Ag deposits, as well as the St. Philippos [51–57] and Pefka [58] polymetallic deposits that have been exploited in the past.

3. Materials and Methods

Ten polished thin sections of magnetite-bearing samples and host rocks were studied by optical and a JEOL JSM 5600 (JEOL Ltd., Tokyo, Japan) scanning electron microscope (SEM) equipped with back-scattered imaging capabilities, at the Department of Mineralogy and Petrology of the University of Athens, Greece. Major and minor elements quantitative analyses on magnetite from three representative samples were carried out at the "Eugen F. Stumpfl" Laboratory, University of Leoben, Austria, using a Jeol Superprobe JXA 8200 (JEOL Ltd., Tokyo, Japan) wavelength-dispersive electron microprobe (WDS). Analytical conditions were as follows: 20 kV accelerating voltage, 10 nA beam current, and 1 μm beam diameter. Peak and backgrounds counting times were 20 s and 10 s for major and 40 s and 20 s for minor and trace elements, respectively. The MgKα, AlKα, SiKα, CaLα, TiKα, VKα, CrKα, FeKα, MnLα, NiLα, and ZnKα X-ray lines were used, with respect to the following standards: corundum for Al, wollastonite for Si and Ca, rutile for Ti, synthetic V for V, chromite for Mg and Cr, natural pyrite for Fe, rhodonite for Mn, NiS for Ni, and natural sphalerite for Zn. Corrections were applied using the PAP online program [59]. Laser ablation ICP-MS analyses of the same samples were conducted at the Institute of Mineralogy, University of Münster, Germany, with a pulsed 193 nm ArF excimer laser (Analyte G2, Photon Machines). A repetition rate of 10 Hz and an energy of ~4 J/cm^2 were used throughout the entire session. The beam spot diameter was set to 35 μm. Trace element analysis has been carried out with an Element 2 mass spectrometer (ThermoFisher). Forward power was 1250 W and reflected power <1 W, gas flow rates were 1.2 L/min for He carrier gas, 0.9 L/m and 1.2 L/m for the Ar-auxiliary and sample gas, respectively. The argon cooling gas flow rate was set to 16 L/min. Before starting an analysis, the system was calibrated to a NIST 612 reference glass measuring ^{139}La, ^{232}Th, and ^{232}Th^{16}O to get stable signals and high sensitivity, as well as low oxide rates (^{232}Th^{16}O/^{232}Th < 0.1%) during ablation. A total of 26 elements (^{25}Mg, ^{27}Al, ^{29}Si, ^{43}Ca, ^{45}Sc, ^{49}Ti, ^{51}V, ^{53}Cr, ^{55}Mn, ^{59}Co, ^{60}Ni, ^{63}Cu, ^{66}Zn, ^{69}Ga, ^{85}Rb, ^{88}Sr, ^{89}Y, ^{90}Zr, ^{93}Nb, ^{95}Mo, ^{118}Sn, ^{137}Ba, ^{178}Hf, ^{181}Ta, ^{182}W, and ^{208}Pb) were quantitatively analyzed using the NIST 612 glass as an external standard while stoichiometric Fe (97% wt.% FeO) was the internal standard, since total concentration of minor elements is <3 wt.% (cf. Milani et al. [60]). Run time of the single ablation pattern was 60 s (20 s for background and 40 s for peak after switching the laser on). Concentrations of measured elements were calculated using

the Glitter software [61,62]. Standard reference glasses BHVO-2G and BIR1-G were analyzed in order to monitor for precision and accuracy during the course of this study. The results from these glasses match the published range of concentrations (standard deviation in the range of 5%), given in the GeoReM database (version 23, [63]).

4. Results

4.1. Geology and Description of the Pagoni Rachi Prospect

The Pagoni Rachi Cu–Mo–Re–Au porphyry prospect lies ca. 18 km NNE of Alexandroupolis. First described by Arikas [64], the Pagoni Rachi porphyry system occurs in an Oligocene granodiorite porphyritic body, which intrudes a Tertiary volcanosedimentary sequence (Figures 1 and 2). This sequence consists of conglomerates, marls, sandstones, and volcaniclastic material (e.g., tuffs) of Priabonian age. It is in turn overlain by volcanic (lava domes and flows) and/or pyroclastic rocks. The northern part of the study area is occupied by a large quartz monzodiorite intrusion, which crosscuts both the volcano-sedimentary sequence and the granodiorite porphyry. The monzodiorite exhibits a medium-grained to porphyritic texture, consisting of plagioclase and various amounts of pyroxene, amphibole, biotite, quartz, and opaques. Radiometric dating for the monzodiorite yielded ages of 31.9 ± 0.5 Ma (Rb/Sr on biotite, [38]). Recently, Perkins et al. [65] provided further geochronological data for the magmatic intrusion in the Kirki area (32.05 ± 0.07 Ma, U–Pb on zircon).

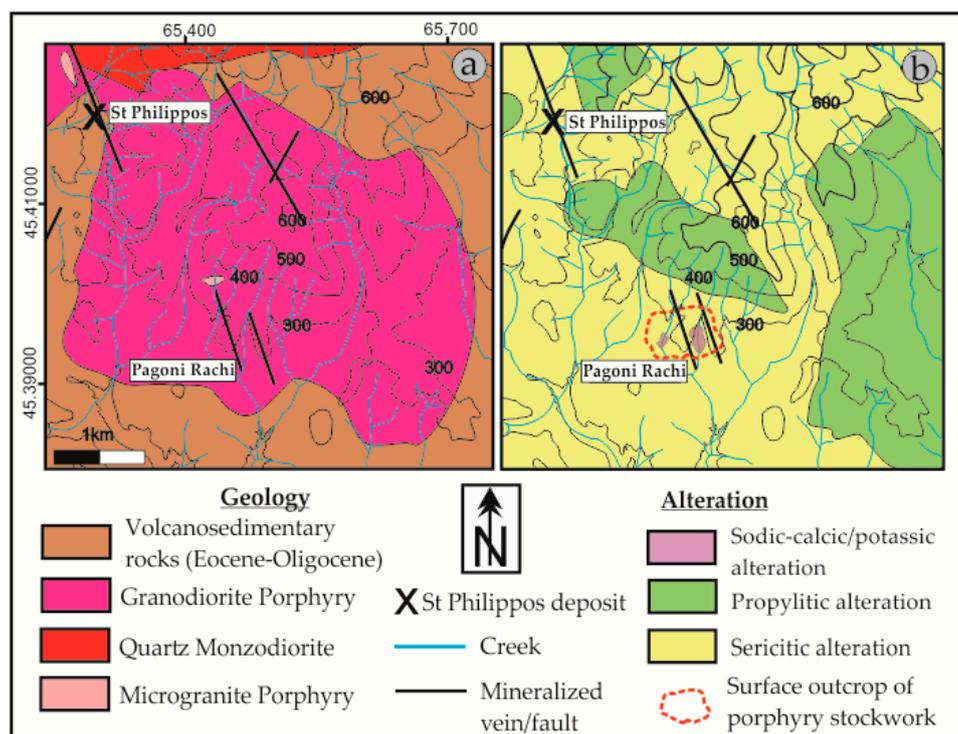**Figure 2.** Geological (**a**) and alteration (**b**) map of the Pagoni Rachi prospect.

Late, NNW-trending microgranite porphyry dikes (Figure 2) crosscut the aforementioned magmatic rocks and comprise the final intrusive stage in the area [51]. These dikes display a porphyritic texture and are composed of coarse-grained resorbed quartz and feldspar phenocrysts; the latter were commonly replaced by sericite, due to pervasive phyllic alteration.

The granodiorite porphyry that hosts the porphyry-style Cu–Mo–Re–Au mineralization is composed of plagioclase, amphibole, biotite, titanite, and scarce resorbed quartz phenocrysts (quartz-eyes), set in a microlitic matrix of quartz, orthoclase, plagioclase, and abundant opaque minerals, mainly magnetite. Mineralization occurs in a very dense quartz stockwork and is associated

with extensive hydrothermal alteration of the granodiorite host (Figure 2b). Late-stage, N- and NW-trending epithermal-style veins crosscut the porphyry mineralization and are associated with argillic (quartz-sericite-carbonates), and, rarely, advanced-argillic (quartz-kaolinite-sericite) alteration selvages, leading to partial telescoping of the porphyry system.

Porphyry-style mineralization has been attributed to four paragenetic stages [51]: (a) early sodic/potassic-calcic alteration associated with magnetite + bornite + chalcopyrite + molybdenite + native gold + quartz veins (M-type veins,) and contemporaneous, distal propylitic alteration; (b) sodic/potassic alteration with pyrite + chalcopyrite + molybdenite + quartz veins (B-type); (c) sericitic alteration with pyrite + chalcopyrite + molybdenite veins (D-type) that also contain native gold along with an important suite of Ag-, Bi-,Te-, and Se-bearing minerals; and (d) argillic alteration with base and precious metal epithermal-style veins (E-type) rich in Au, Ag, and Te. Mineralogical similarities of these veins suggest that they may share a genetic relationship with the D-type veins. Bulk ore chemical analyses of surface samples showed that the system is significantly enriched in Cu (up to 0.5 wt.%), Mo (up to 2000 ppm), Au (up to 5 ppm), and Re (up to 20 ppm). The extreme rhenium enrichment of the Pagoni Rachi system reflects the presence of the rare sulfide rheniite and Re-rich molybdenite [50,51].

4.2. Modes of Magnetite Occurrence (Petrography)

Following the textural and morphological criteria proposed by McQueen and Cross [66] and Nadoll et al. [14], magnetite in the Pagoni Rachi porphyry-style mineralization occurs in two distinct types:

The first type, hereafter called as magmatic magnetite, occurs in fresh to propyliticaly altered granodiorite porphyry (Figure 3a–c). Primary magnetite (Figure 4a–d) usually forms relatively large (up to 0.2 cm), euhedral to subhedral crystals (octahedral, cubo-octahedral habits) that are randomly scattered in the matrix of the rock, and which exhibit a characteristic porphyritic texture (Figure 4). It comprises the most abundant opaque accessory phase (approx. 5% modal) and is associated with the primary silicate minerals of the granodiorite. Commonly propylitic alteration is present; in this case magnetite is set in a matrix of relict primary minerals replaced by variable amounts of secondary epidote, albite, actinolite, chlorite, and calcite (Figure 4a,b).

In such cases, magnetite is commonly replaced by hematite (martitization, Figure 4b) in the periphery of the crystals or along fractures. Rare exsolution lamellae (trellis-type) of ilmenite, typical for magmatic magnetite (cf. Wen et al. [17]) were identified (Figure 4d), at places also replaced by hematite.

The second type of magnetite is secondary (hereafter called "hydrothermal") and (Figures 3c–f and 5) is only found in the central part of the studied porphyry mineralization and is associated with sodic-potassic/calcic alteration. Its modal abundance (more than 10%) is significantly higher compared to its magmatic counterpart in the fresh to propylitic-altered granodiorite.
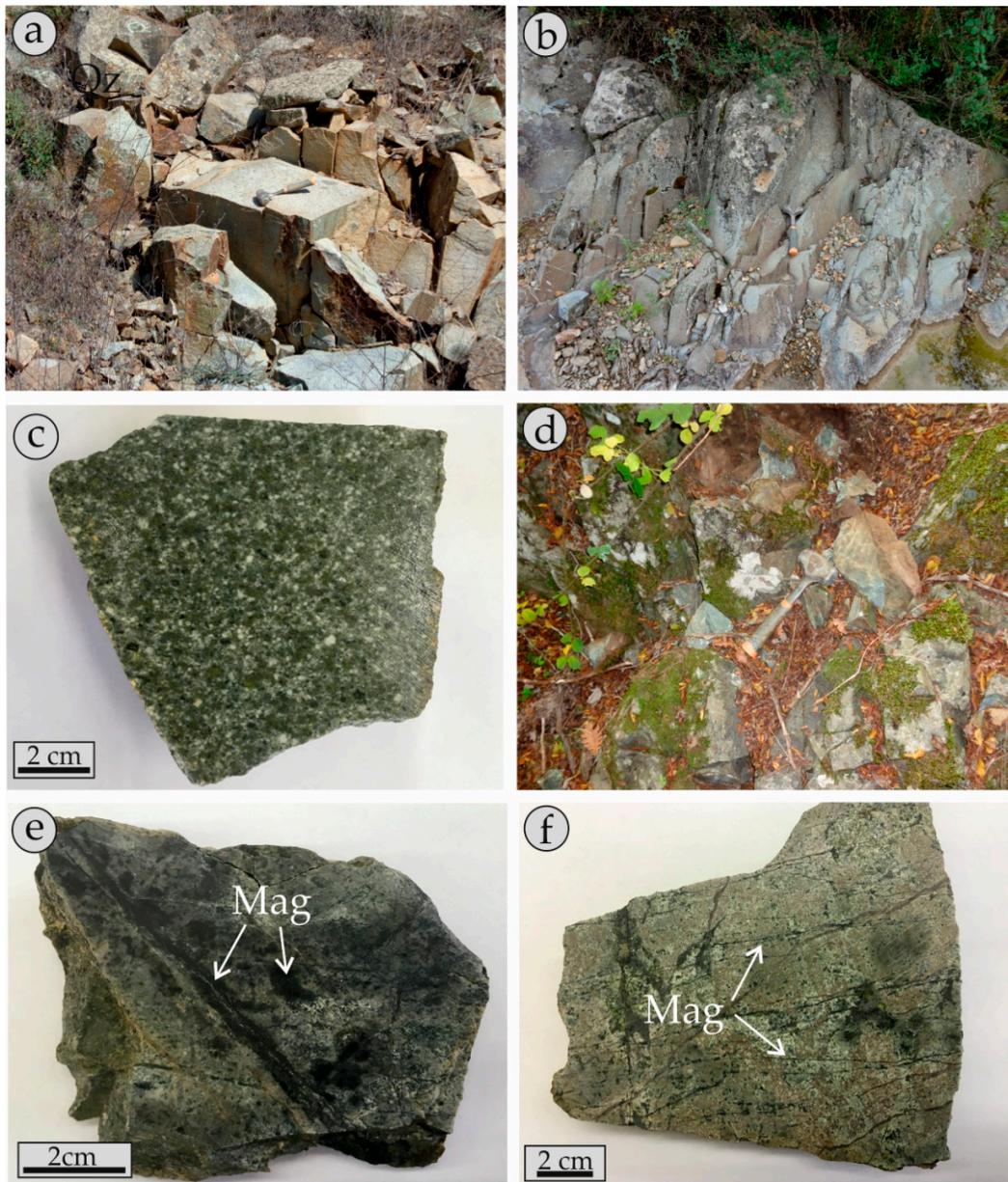
Figure 3. Field and hand-specimen photographs of magnetite-bearing rocks from the Pagoni Rachi prospect: (**a**–**c**) fresh to propylitic altered granodiorite porphyry; and (**d**–**f**) sodic–potassic/calcic altered granodiorite porphyry crosscut by hydrothermal magnetite veinlets (M-type).
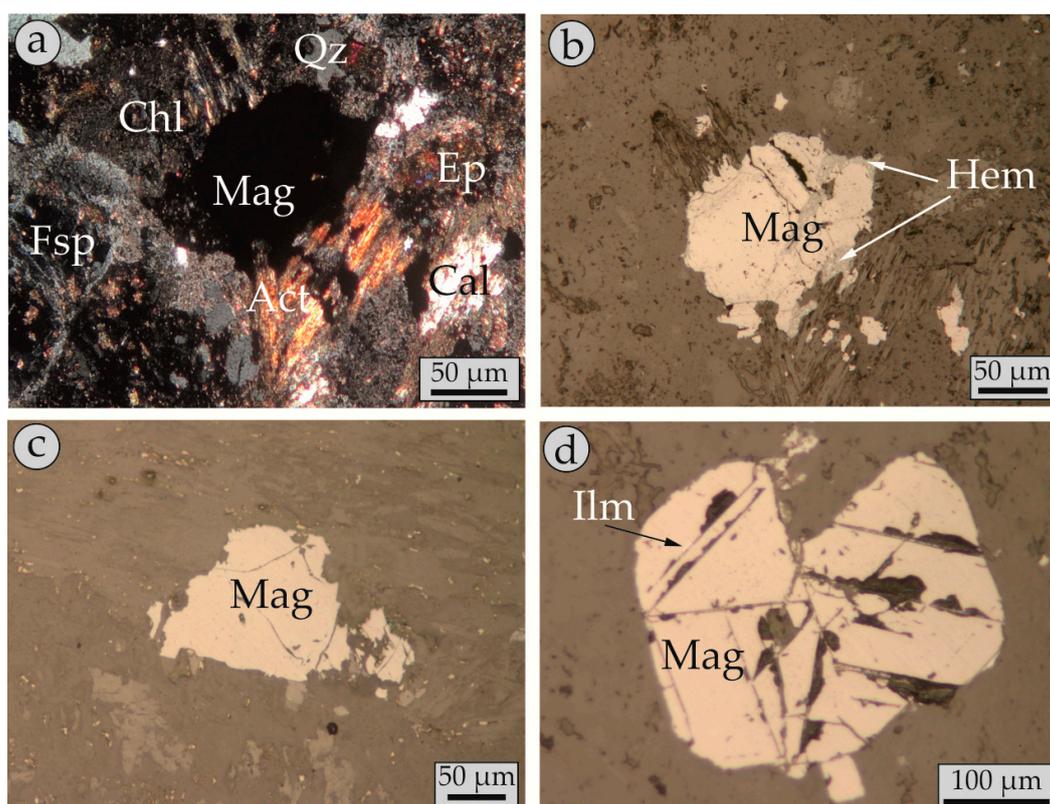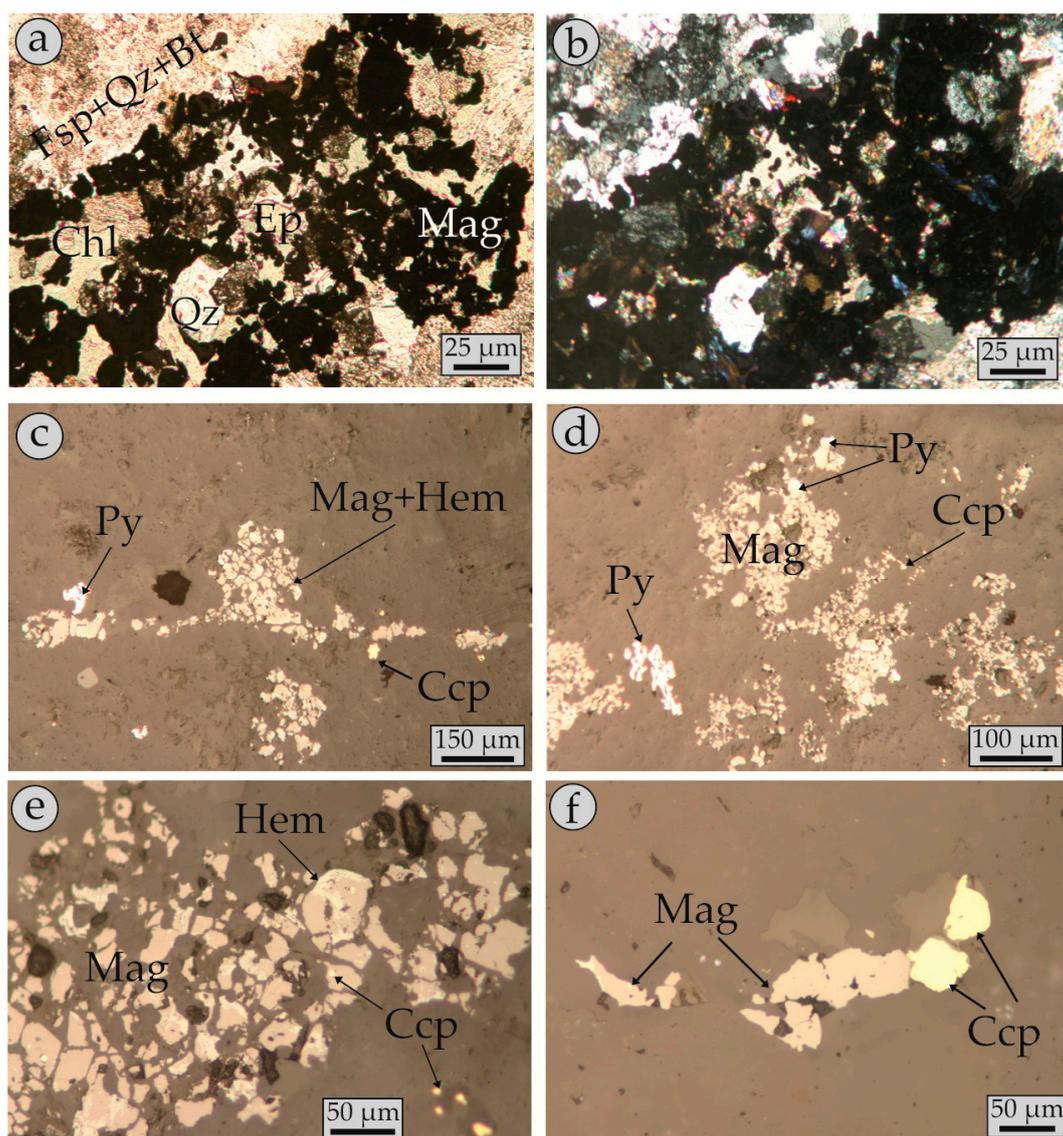
Figure 4. Transmitted (**a**) and reflected (**b**–**d**) light microphotographs of magmatic magnetite from fresh to propylitic-altered granodiorite porphyry: (**a**) magnetite (Mag) grain, set in a propylitic matrix consisting of plagioclase replacing feldspar (Fsp), actinolite (act), epidote (ep), quartz (Qz), calcite (Cal), and chlorite (chl), (crossed-polarized light); (**b**) the same grain as in (**a**). Note the partial replacement of magnetite by hematite (Hem); (**c**) subhedral magnetite grain; and (**d**) euhedral magnetite grain showing minor exsolution lamellae of ilmenite (Ilm).

Hydrothermal magnetite forms a complex network of dark-colored veinlets set in a greenish to brown-colored matrix of secondary minerals. Moreover, magnetite may also be present in granular wavy to locally straight-sided quartz veins (A-type), which lack alteration selvages. Rarely, aggregates of magnetite occur in the sodic-potassic/calcic altered matrix.

This style of alteration (sodic-potassic/calcic) has totally obliterated the igneous porphyritic texture of the granodiorite and resulted in its complete recrystallization. It is composed of variable amounts of secondary albite, orthoclase, biotite, actinolite, and chlorite. The veinlets (M-type) are commonly very narrow (less than 0.5 cm), irregular in shape and discontinuous, but there are also cases where straight-sided veinlets were identified.

Magnetite in the veins is commonly anhedral, has a grain size that does not exceed a few tens of microns, and may contain (sub-) microscopic inclusions of silicates (e.g., titanite) and/or sulfides (e.g., chalcopyrite). It is associated with variable amounts of orthoclase, biotite, albite, chlorite, actinolite, and quartz (Figure 5a–b). Minor chalcopyrite and pyrite accompany magnetite in the veins (Figure 5c–e) along with minor amounts of bornite, gold, and molybdenite. In places, replacement features occurred (martitization) whereas exsolution lamellae were absent.

Figure 5. Transmitted (**a**,**b**) and reflected (**c**–**f**) light microphotographs of hydrothermal magnetite from M-type veinlets cross-cutting sodic-calcic/potassic altered granodiorite porphyry: (**a**,**b**) subhedral to anhedral magnetite grains forming aggregates set in a matrix consisting of albite and orthoclase (Fsp), epidote (Ep), biotite (bt), chlorite (Chl), and quartz (Qz; plane- and crossed-polarized light, respectively); (**c**–**e**) Subhedral to anhedral magnetite associated with hematite (Hem), pyrite (Py), and chalcopyrite (Ccp).

4.3. Chemical Composition of Magnetite

Analytical data from both magmatic and hydrothermal magnetite are shown in Tables 1 and 2 for the Electron Probe Microanalyses (EPMA) and LA-ICP-MS analyses, respectively. Chemical differences between the two types of magnetite are displayed in covariation plots of Figure 6.

Electron probe micro-analyses of magmatic magnetite show that Ti was the major impurity, reaching up to 2.77 wt.% TiO_2 (average 1.41 wt.%). Despite this relatively broad range, no zoned structure was observed. Silica (up to 0.52 wt.%) and Ca (up to 0.34 wt.% CaO) were the next most abundant elements. The majority of other divalent (e.g., Mg and Mn) and trivalent (e.g., Al and Cr) cations that could be incorporated into the structure of magnetite were mostly very close to, or below detection limits, with the exception of V, with values of up to 0.28 wt.% V_2O_3.

Table 1. EPMA data of magmatic and hydrothermal magnetite from the Pagoni Rachi prospect.

Sample	KM81			KM68			KM74		
Type	Magmatic (*n* = 15)			Hydrothermal (*n* = 29)			Hydrothermal (*n* = 30)		
(wt %)	avg	min	max	avg	min	max	avg	min	max
MgO	0.01	bdl	0.03	0.01	bdl	0.24	0.01	bdl	0.88
CaO	0.05	0.02	0.34	0.04	bdl	0.07	0.03	bdl	0.23
MnO	0.01	bdl	0.18	0.01	bdl	0.10	0.01	bdl	0.32
FeO$_{tot}$	97.10	95.44	98.69	97.94	96.88	98.40	98.11	97.03	99.19
TiO$_2$	1.41	1.05	2.77	0.39	0.20	0.78	0.47	0.11	1.13
Al$_2$O$_3$	0.04	bdl	0.58	0.16	0.22	0.46	0.05	bdl	0.17
SiO$_2$	0.06	bdl	0.52	0.07	bdl	0.30	0.05	bdl	0.18
Cr$_2$O	0.02	0.01	0.08	0.02	bdl	0.04	0.01	bdl	0.06
NiO	0.01	bdl	0.04	0.01	bdl	0.06	0.02	bdl	0.07
ZnO	0.01	bdl	0.05	0.04	0.03	0.18	0.01	bdl	0.03
V$_2$O	0.16	bdl	0.28	0.21	0.05	0.32	0.22	0.09	0.33
Total	97.70	98.04	99.13	98.87	97.01	99.41	98.85	94.71	99.28

n = number of analyses; tot = total; avg = average value; min = minimum value; max = maximum value; bdl = below detection limit.

Table 2. Laser ablation-inductively coupled plasma-mass spectrometry (LA-ICP-MS) data of magmatic and hydrothermal magnetite from the Pagoni Rachi prospect.

Sample	KM81			KM68			KM74		
Type	Magmatic (*n* = 12)			Hydrothermal (*n* = 15)			Hydrothermal (*n* = 15)		
(ppm)	avg	min	max	avg	min	max	avg	min	max
Mg	1271	612	2678	2643	550	6896	2043	451	3613
Al	5679	4112	7845	5131	3354	5977	4676	2002	6808
Si	3120	991	8521	3376	1338	6247	4481	1982	6679
Ca	1755	740	4125	1386	980	2065	2749	910	4158
Sc	3	2	4	4	1	18	12	4	23
Ti	20,179	9915	22,545	3202	1200	4852	2419	1305	11,517
V	561	395	770	1777	1622	1968	1784	1077	3079
Cr	329	221	454	20	16	25	23	14	28
Mn	316	224	412	1047	637	2199	954	412	2672
Co	22	19	27	12	3	21	7	4	14
Ni	23	19	31	16	12	21	16	14	19
Cu	5	2	8	56	bdl	156	21	bdl	152
Zn	51	33	79	189	1417	2163	2926	1860	4004
Ga	15	9	22	17	11	35	34	31	40
Rb	3	2	5	2	bdl	7	4	bdl	19
Sr	6	4	8	11	2	30	18	bdl	72
Y	10	4	14	11	1	53	1	bdl	10
Zr	15	4	24	1	bdl	10	4	bdl	23
Nb	4	1	9	8	bdl	55	10	bdl	40
Mo	1	bdl	2	4	1	9	3	1	6
Sn	64	36	99	13	5	39	35	26	41
Ba	6	2	11	5	3	8	4	bdl	11
Hf	0.3	bdl	1.2	0.2	bdl	1	0.4	bdl	2
Ta	bdl	bdl	1	1	bdl	7	1	bdl	3
W	2	1	4	6	bdl	44	3	bdl	9
Pb	21	12	36	49	10	128	6	bdl	20

n = number of analyses; avg = average value; min = minimum value; max = maximum value; bdl = below detection limit.

On the other hand, hydrothermal magnetite contained significantly less TiO$_2$ (up to 0.78 wt.% and 1.13 wt.% in the two samples respectively) compared to the magmatic one, but had relatively

elevated contents of Mg, Mn, and V (values up to 0.88 wt.% MgO, 0.32 wt.% MnO, and 0.33 wt.% V_2O_3, respectively). Most of the other trace elements were close to or below the detection limit of the method (Table 1). Zonation features were not observed.

Laser ablation-inductively coupled plasma mass-spectrometry analyses yielded comparable results to those obtained through EPMA: Ti values in the two hydrothermal magnetite-bearing samples that reach up to 4852 ppm and 11,517 ppm Ti (average values 3202 ppm and 2419 ppm respectively), and were much smaller compared to those in magmatic magnetite, which contained up to 22,545 ppm (average 9915 ppm). Alumina, Si, and Ca values are up to 7845 ppm (average 4112 ppm), 8521 ppm (average 991 ppm), and 4125 ppm (average 740 ppm) respectively. It must be noted that the maximum values in these elements corresponded to the same analytical spots, which might reflect the presence of sub-millimetric or nano-scale silicate inclusions at subsurface during ablation (cf. Deditius et al. [67]).

The average Mg content of the two types of magnetite was approximately the same (612 ppm for magmatic magnetite and 451 ppm and 550 ppm for the two hydrothermal magnetite samples. Maximum values were much higher (up to 2678 ppm in the magmatic sample and 6896 ppm and 3613 ppm in the two hydrothermal samples.

Vanadium was enriched in the hydrothermal magnetite. Maximum values ranged between 1968 ppm (average 1622 ppm) and 3079 ppm (average 1077 ppm) in the two samples, whereas maximum values in the magmatic magnetite was 770 ppm (average 395 ppm).

A similar trend was the case for most trace elements (Table 2): hydrothermal magnetite was enriched in high-field strength elements (e.g., Nb, Hf, Ta, and W) and metals (e.g., Cu, Zn, and Mo).

On the other hand, some elements were preferably enriched in the magmatic magnetite: the Co of magmatic magnetite was slightly higher (up to 27 ppm) than that of the hydrothermal ones (up to 21 ppm). Other enriched elements were Cr (up to 454 ppm in magmatic; and up to 28 ppm in hydrothermal magnetite respectively), Ni (up to 31 ppm in magmatic and up to 21 ppm in hydrothermal magnetite), and Sn (up to 99 ppm in magmatic and up to 41 ppm in hydrothermal magnetite).

Differences in the concentrations observed between EPM and LA-ICP-MS analyses for elements like Ti, Mg, Cr, Ca, and Si was attributed to the variation of the beam-size of the two methods, especially when exsolved phases or micro-inclusions were present in the magnetite. Furthermore, elevated contents acquired by LA-ICP-MS analyses (e.g., values of Si, Ca, Ti, and Al) might suggest that at least some of the very high concentrations was due to unavoidable submicroscopic or nano-scale inclusions of silicates.

5. Discussion

Magnetite is a common mineral in porphyry deposits. Magnetite of magmatic origin is commonly disseminated in the unaltered intrusive rocks or partly as a relict in propylitic alteration that surrounds the mineralized center [14,18]. The composition of magnetite seems to be a function of several factors including temperature, fS_2 and/or fO_2, cooling rate, melt composition, and element partitioning between co-precipitating phases [1,2,12,13,16,68]. Available experimental data on igneous magnetite have shown that its composition depends mainly on the temperature of crystallization, the fS_2 and fO_2 conditions, and buffering between melt and the host rock [69–71]. For instance, an increase in oxygen fugacity would reduce the solubility of Ti in magnetite and consequently cause oxy-exsolution of ilmenite (cf. Wen et al. [17]).

In contrast, hydrothermal magnetite is usually common in early, high-temperature stages associated with potassic alteration assemblages at the cores of the systems [13–15,18]. Here, elemental availability in the hydrothermal fluid seems to be a critical component that determines its composition, combined with temperature, sulfur and oxygen fugacities, and fluid-rock interaction [13]. Although present in the majority of the porphyry-style deposits, there seems to be a greater abundance of magnetite in gold-rich deposits, a feature that could be attributed to the generation of such deposits by more oxidizing magmas [72,73]. Iron in the porphyry environment is usually thought to be transported

as a chloride complex in a magmatic vapor ($FeCl_2$) and magnetite is considered to precipitate as a result of volatile exsolution at relatively high temperature and pressure conditions [74].

## 5.1. Fingerprinting Magmatic and Hydrothermal Processes

The Ti versus Ni/Cr discrimination diagram of Dare et al. [1] distinguishes the two types of magnetite in the Pagoni Rachi prospect (Figure 6a), as magmatic magnetite has high Ti and low Ni/Cr values compared to its hydrothermal counterpart. Furthermore, the Ti versus Al plot, proposed by Canil et al. [15], also distinguishes the studied magnetite, but mostly based on Ti content, since their Al content is relatively constant (Figure 6b) in both magmatic and hydrothermal magnetite.

The significant enrichment of V in magnetite of the Pagoni Rachi prospect is a feature previously described from other porphyry deposits elsewhere (e.g., [14,15,18]). Vanadium in the Pagoni Rachi is present in both types of magnetite, but its concentration is higher in the hydrothermal grains (Figure 6c). Vanadium is characterized by significant mobility even in low temperature hydrothermal fluids [75]. Its presence, commonly is in the trivalent state, since it has a similar ionic radius to Fe^{3+} [69], is a function of oxygen fugacity of the hydrothermal fluid as well as of the presence of any other co-existing minerals with magnetite, which can also incorporate V^{3+} (e.g., ilmenite and biotite). Since V is enriched in the hydrothermal type of magnetite from Pagoni Rachi, its availability in the hydrothermal fluid could be strengthened by dissolution of V-rich magmatic magnetite. This procedure could result in reprecipitation of newly-formed hydrothermal magnetite that has partly inherited features of its magmatic counterpart, as described by Wen et al. [17]. The two types of magnetite in the Pagoni Rachi prospect are partly discriminated in the plot of Ca + Al + Mn versus Ti + V plot (Figure 6d), although it should be noted here that composition of magnetite regardless of its origin in the prospect overlaps the genetic fields defined by Dupuis and Beaudoin [7] and Nadoll and Koenig [76].

Figure 7 graphically represents the chemical composition of magmatic and hydrothermal magnetite analyzed during the present study. In Figure 7a, the average composition of the two varieties of magnetite from Pagoni Rachi, normalized to bulk composition of the continental crust, plot along with the compositional range of high-temperature hydrothermal magnetite of Dare et al., [1]. With the exception of Ti, Sn, and Cr, most elements are enriched in the hydrothermal magnetite. The concentrations of Si and Ca from both types of magnetite in the Pagoni Rachi prospect are higher than those reported by Dare et al. [1] for hydrothermal magnetite. In general, magmatic magnetite is depleted in both elements, since they are considered to be incompatible, when igneous magnetite crystallizes from silicate melts [12].
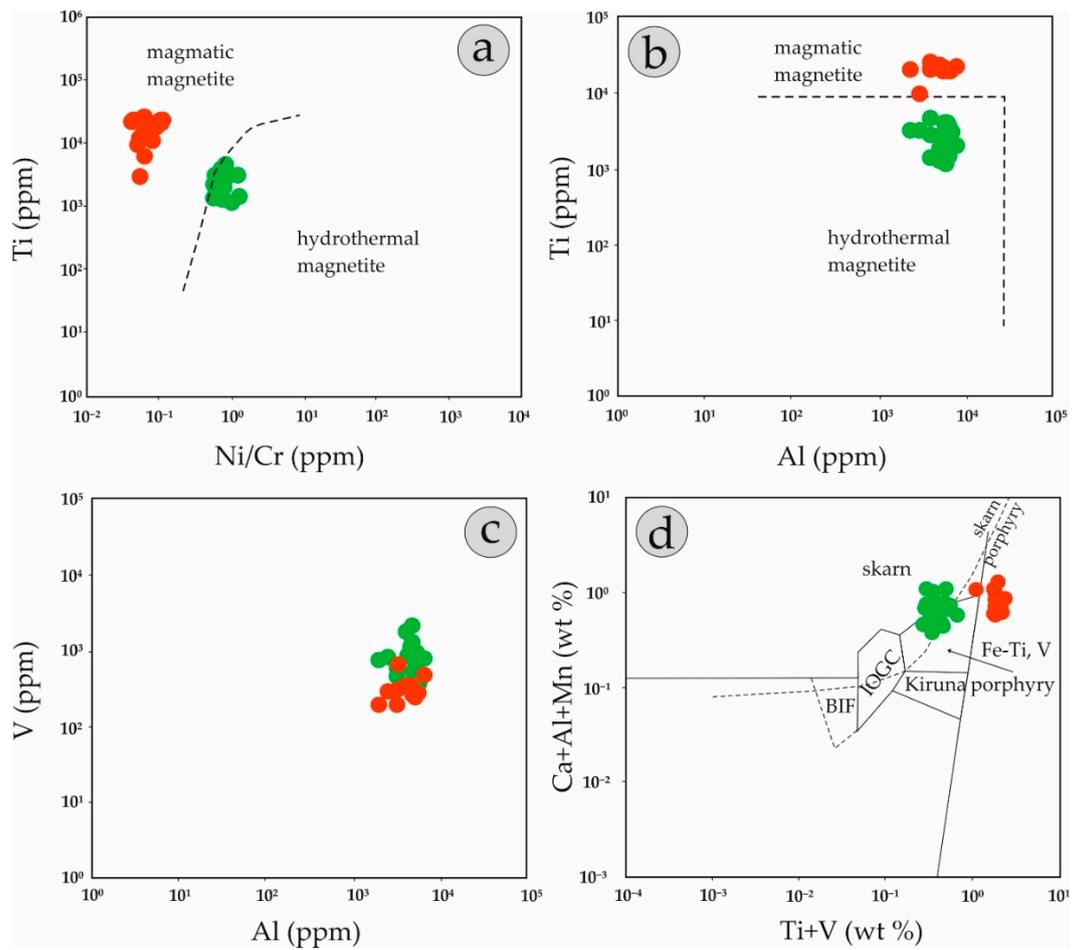
Figure 6. Covariation plots of magmatic (red symbols) and hydrothermal (green symbols) magnetite from the Pagoni Rachi porphyry prospect: (**a**) Ti versus Ni/Cr ratio (fields after Dare et al. [1]); (**b**) Til versus Al (fields after Canil et al. [15]); (**c**) V versus Al; and (**d**) Ca + Al + Mn versus Ti + V (fields after Dupuis and Beaudoin [7] and Nadoll and Koenig [76]).
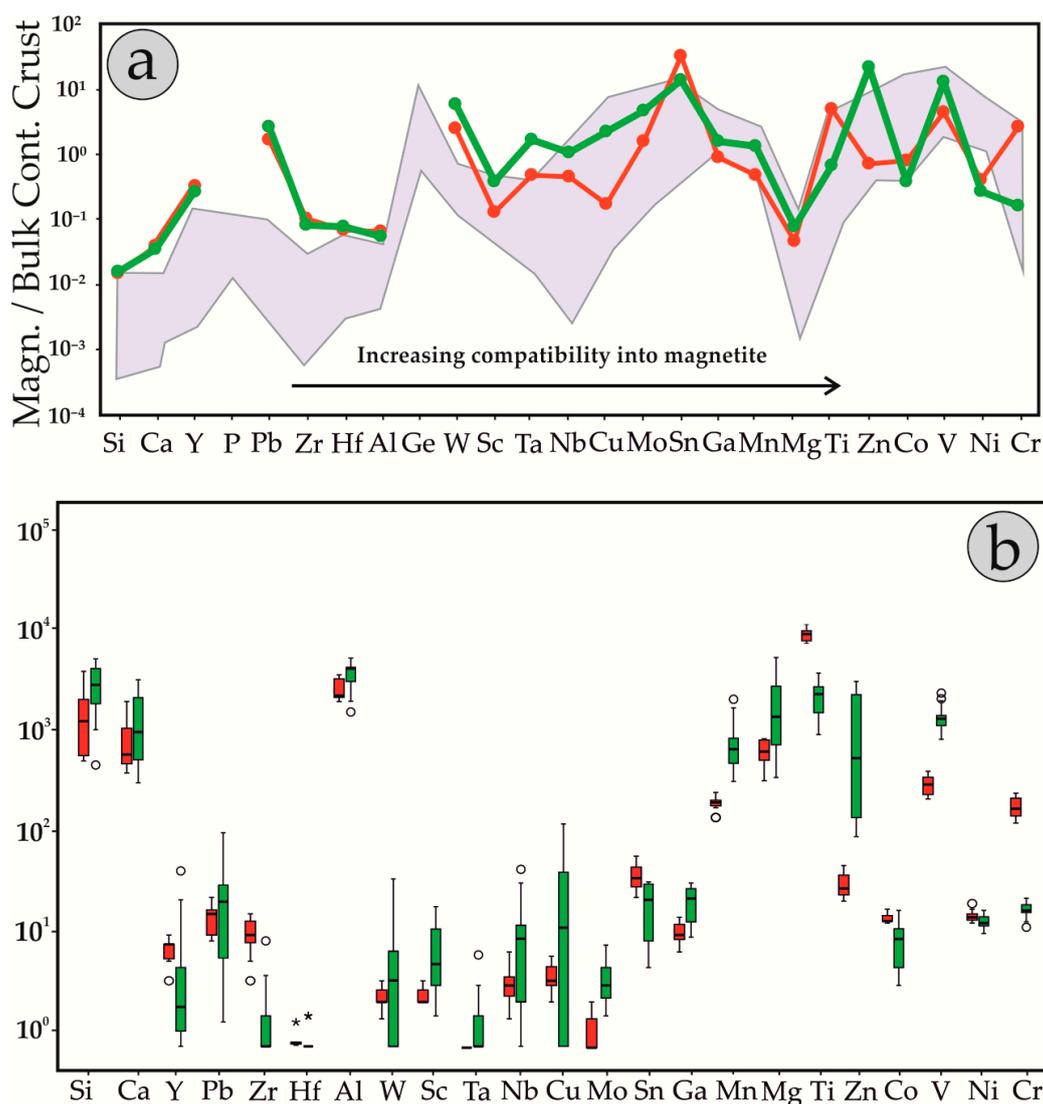
Figure 7. Chemical variation diagrams of magmatic (red) and hydrothermal (green) magnetite from the Pagoni Rachi porphyry prospect (values in ppm): (**a**) Multi-element plot of average trace element composition of magmatic and hydrothermal magnetite, normalized to bulk continental crust (values after Rudnick and Gao [77]; grey field represents the compositional range of high-temperature hydrothermal magnetite, after Dare et al. [1]) and (**b**) box and whisker plot of various trace elements in magmatic (red boxes) and hydrothermal (green boxes) magnetite for the Pagoni Rachi porphyry prospect, analyzed by LA-ICP-MS. The upper and lower margins of the boxes represent the upper and lower 75% and lower 25% of the data respectively. The whiskers represent upper and lower threshold values (95% of the data), while median values are shown as thick black lines inside the boxes. Open circles and stars represent extreme values. Maximum values of Si, Al, Mg, and Ca attributed to inclusions have been excluded.

On the other hand, hydrothermal magnetite may carry significant amounts of Si and Ca, as both elements are highly mobile during hydrothermal alteration. Silicon- and Ca-rich magnetite have been reported from several deposits, commonly skarns (e.g., [78]). In the case of the Pagoni Rachi porphyry prospect, significant Si-Ca mobility during alteration has been well documented, as hydrothermal magnetite is accompanied by Ca-rich mineral assemblages (e.g., hydrothermal actinolite, Voudouris et al. [50,51]). Moreover, very high values of these two elements, when they correlate along high Ti values (Figure 8) are likely due to the presence of nano-scale inclusions of titanite (cf. Deditius et al. [67]).
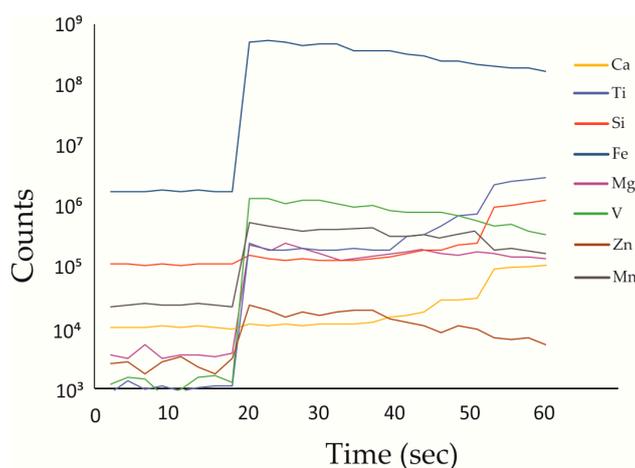
Figure 8. Time resolved analytical profile on a grain of hydrothermal magnetite. The increase of Si, Ca, and Ti values implies the intersection of nano-scale titanite inclusion.

Magnesium and less commonly Mn can be enriched in hydrothermal magnetite, due to extensive fluid-rock interactions [79,80]. Such interactions enriched both elements in the studied magnetite and could easily be explained by the mafic component of the hosting granodioritic intrusion.

With the exception of Zr and Hf, which displayed relatively constant concentrations both in magmatic and hydrothermal magnetite, other high-field strength elements were preferably enriched in the hydrothermal magnetite (Figure 7b). As most of these elements were incompatible in magnetite, they were relatively immobile and tend to be incorporated in late magmatic magnetite. Their solubility in hydrothermal fluids is restricted [81–83]. However, the enrichment of elements like W, Mo, Ta, and Nb in the hydrothermal magnetite could indicate that it precipitated from a hydrothermal fluid that derived from a felsic intrusion and contained a significant amount of such elements. Large variation in their concentration could imply that they were incorporated in the magnetite grains following an inhomogeneous distribution.

The copper content of magmatic magnetite was very low, but a significant enrichment was present in the hydrothermal variety. Copper-rich magnetite is common in many porphyry-style deposits, with extreme values of a few thousands of ppm (e.g., magnetite from Mt Polley porphyry deposit, [18]), but its origin is still a matter of debate, as the presence of nano-scale inclusions of copper sulfides cannot be ruled out (e.g., [84]).

Lead enrichment is an important feature of magnetite from Pagoni Rachi. Minor amounts of Pb were present in the magmatic magnetite, and could be explained by its weakly compatible behavior (D_{Pb} = 1.4 in magmatic magnetite). The Pb content rose significantly in the hydrothermal type of magnetite: given the fact that Pb is a chalcophile element, and is preferably incorporated in coexisting Fe–Cu sulfides (e.g., [1]), its presence in hydrothermal magnetite suggests enrichment of this element in the parental hydrothermal fluid, that is exsolved from a felsic magmatic source, as also described by Huang et al., [16].

Another notable feature of the studied magnetite is their enrichment in Sn, which is obvious in both types of magnetite but is larger in the igneous magnetite. Analogous enrichment of Sn in porphyry-related magnetite was reported previously from the Endako porphyry-Mo deposit [85], which is hosted in granitoids, which are notably more felsic compared to the granodiorite hosting the Pagoni Rachi prospect.

5.2. Genetic Considerations—Implications for Exploration

Although hosted in an intermediate magmatic body with high-K calc-alkaline affinity, the Pagoni Rachi porphyry prospect was characterized by a number of features that point towards a genetic relation to a more evolved, felsic intrusive phase. This inquiry has already been stated by Voudouris et al. [51],

who discussed the possibility of a genetic relationship between the porphyry system and a buried granitic intrusion similar to that exposed at the nearby St. Philippos deposit. Furthermore, the presence of fluorite as a gangue mineral in the quartz porphyry veins of the Pagoni Rachi [51], as well as the enrichment of F and Cl in secondary biotite (C. Mavrogonatos unpublished data) from the sodic/potassic-calcic alteration of the system, also suggest a strong affinity with a halogen-enriched hydrothermal fluid derived from a felsic magma.

High-field strength elements, which are enriched in secondary magnetite, suggest elevated mobility during hydrothermal alteration. Such enrichment has been described previously from fluoride-rich magmatic systems, especially of alkaline character [86]. Moreover, as has been shown by experimental studies, even the presence of a minor amount of base metals like Mn and Zn in hydrothermal magnetite, reflects an elevated concentration of these elements in chloride-rich hydrothermal fluids, which suggest an enrichment caused by fluid-rock interactions [78,79].

Significant porphyry-style mineralization hosted in microgranite, has already been described from the Thrace metallogenic district, thus documenting a genetic link between porphyry-style prospects and the microgranitic magmatism (e.g., the Maronia porphyry Cu–Mo–Re–Au [53] and the Aisymi-Leptokarya porphyry Mo [45,54] systems). The existence of microgranitic bodies in the Pagoni Rachi area, as well as the presence of F-rich phases in advanced argillic alteration assemblages in epithermal-style mineralization [31,48,49], locally superimposed on the porphyry-style ores in the broad area, is also compatible with a deep, large-scale microgranitic intrusion, which could (at least partly) control the alteration styles and contribute to the metal endowment of the Pagoni Rachi porphyry prospect.

Further studies of trace elements in magnetite from other deposits and prospects in the district will increase our knowledge concerning their distribution during ore formation and will help to determine a trace element pattern that could be used as a vector towards ore-grade mineralized centers in the Thrace metallogenic district.

6. Conclusions

Magnetite occurs as two modes of occurrence in the Pagoni Rachi porphyry Cu–Mo–Re–Au prospect. The first, recognized as magmatic-type, is present in fresh to propylitic-altered granodiorite porphyry, peripherally to the mineralized center of the system. The second type of magnetite, which is of hydrothermal origin, is found in the core of the system, associated with sodic/potassic-calcic alteration of the host rock. Magmatic magnetite forms subhedral to euhedral grains, with sizes up to 0.2 cm. In places, rare trellis-type exsolution lamellae of ilmenite may occur. Hydrothermal magnetite occurs as narrow veinlets (M-type) or within sinuous quartz veins (A-type), forming fine, anhedral grains. It is associated with various amounts of secondary biotite, K-feldspar, and/or albite, actinolite, and chlorite.

Trace element analyses revealed significant differences in the composition of the two types of magnetite. Magmatic magnetite from Pagoni Rachi, similar to magmatic magnetite from intrusions related to ore deposits elsewhere, was characterized by elevated concentrations of Ti, Cr, Ni, and Sn. In contrast, high-field strength elements and metals were preferably enriched in the hydrothermal magnetite. In addition, enrichment in Zn, Pb, W, Ta, and Mo was a distinctive feature of the Pagoni Rachi hydrothermal magnetite. Very high values of Si, Ca, Mg, and Al might indicate submicroscopic and/or nano-scale inclusions in hydrothermal magnetite.

The trace elements pattern of the hydrothermal magnetite could be further tested as an exploration tool towards ore-grade mineralization in other fertile intrusions in NE Greece, which share similar genetic features to Pagoni Rachi (e.g., causative intrusion and metal endowment, similar alteration assemblages, etc.).

Conflicts of Interest: The authors declare no conflict of interest.

References

1. Dare, S.A.S.; Barnes, S.-J.; Beaudoin, G.; Méric, J.; Boutroy, E.; Potvin-Doucet, C. Trace elements in magnetite as petrogenetic indicators. *Minim. Depos.* **2014**, *49*, 785–796. [CrossRef]
2. Sack, R.O.; Ghiorso, M.S. Chromian spinels as petrogenetic indicators: Thermodynamics and petrological applications. *Am. Mineral.* **1991**, *76*, 827–847.
3. Roeder, P.L. Chromite: From the fiery rain of chondrules to the Kilauea Iki lava lake. *Can. Mineral.* **1994**, *32*, 729–746.
4. Barnes, S.J.; Roeder, P.L. The range of spinel compositions in terrestrial mafic and ultramafic rocks. *J. Pet.* **2001**, *42*, 2279–2302. [CrossRef]
5. Nadoll, P.; Mauk, J.L.; Hayes, T.S.; Koenig, A.E.; Box, S.E. Geochemistry of magnetite from hydrothermal ore deposits and host rocks of the Mesoproterozoic Belt Supergroup, United States. *Econ. Geol.* **2012**, *107*, 1275–1292. [CrossRef]
6. Chen, W.; Ying, Y.C.; Bai, T.; Zhang, J.J.; Jiang, S.Y.; Zhao, K.D.; Shin, D.; Kynicky, J. In situ major and trace element analysis of magnetite from carbonatite-related complexes: Implications for petrogenesis and ore genesis. *Ore Geol. Rev.* **2019**, *107*, 30–40. [CrossRef]
7. Dupuis, C.; Beaudoin, G. Discriminant diagrams for iron oxide trace element fingerprinting of mineral deposit types. *Minim. Depos.* **2011**, *46*, 319–335. [CrossRef]
8. Liu, Y.S.; Hu, Z.C.; Gao, S.; Günther, D.; Xu, J.; Gao, C.G. In situ analysis of major and trace elements of anhydrous minerals by LA-ICP-MS without applying an internal standard. *Chem. Geol.* **2008**, *257*, 34–43. [CrossRef]
9. Wijbrans, C.H.; Klemme, S.; Berndt, J.; Vollmer, C. Experimental determination of trace element partition coefficients between spinel and silicate melt: The influence of chemical composition and oxygen fugacity. *Contrib Mineral. Petrol.* **2015**, *69*, 45–77. [CrossRef]
10. Müller, B.; Axelsson, M.D.; Ohlander, B. Trace elements in magnetite from Kiruna, northern Sweden, as determined by LA-ICP-MS. *GFF* **2003**, *125*, 1–5. [CrossRef]
11. Carew, M.J. Controls on Cu–Au Mineralisation and Fe-Oxide Metasomatism in the Eastern Fold Belt, NW Queensland, Australia. Ph.D. Thesis, James Cook University, Townsville, Australia, 2004.
12. Dare, S.A.S.; Barnes, S.-J.; Beaudoin, G. Variation in trace element content of magnetite crystallized from a fractionating sulfide liquid, Sudbury, Canada: Implications for provenance discrimination. *Geochim. Cosmochim. Acta* **2012**, *88*, 27–50. [CrossRef]
13. Nadoll, P.; Angerer, T.; Mauk, J.L.; French, D.; Walshe, J. The chemistry of hydrothermal magnetite: A review. *Ore Geol. Rev.* **2014**, *61*, 1–32. [CrossRef]
14. Nadoll, P.; Mauk, J.L.; Leveille, R.A.; Koenig, A.E. Geochemistry of magnetite from porphyry Cu and skarn deposits in the southwestern United States. *Miner. Depos.* **2015**, *50*, 493–515. [CrossRef]
15. Canil, D.; Grondahl, C.; Lacourse, T.; Pisiak, L.K. Trace elements in magnetitefrom porphyry Cu-Mo-Au deposits in British Columbia, Canada. *Ore Geol. Rev.* **2016**, *72*, 1116–1128. [CrossRef]
16. Huang, X.W.; Sappin, A.A.; Boutroy, E.; Beaudoin, G.; Makvandi, S. Trace Element Composition of Igneous and Hydrothermal Magnetite from Porphyry Deposits: Relationship to Deposit Subtypes and Magmatic Affinity. *Econ. Geol.* **2019**, *114*, 917–952. [CrossRef]
17. Wen, G.; Li, J.W.; Hofstra, A.H.; Koenig, A.E.; Lowers, H.A.; Adams, D. Hydrothermal reequilibration of igneous magnetite in altered granitic plutons and its implications for magnetite classification schemes: Insights from the Handan-Xingtai iron district, North China Craton Guang. *Geochim. Cosmochim. Acta* **2017**, *213*, 255–270. [CrossRef]

18. Pisiak, L.K.; Canil, D.; Lacourse, T.; Plouffe, A.; Ferbey, T. Magnetite as an indicator mineral in the exploration of porphyry deposits: A case study in till near the Mount Polley Cu-Au deposit, British Columbia, Canada. *Econ. Geol.* **2017**, *112*, 919–940. [CrossRef]

19. Averill, S.A. The application of heavy indicator mineralogy in mineral exploration with emphasis on base metal indicators in glaciated metamorphic and plutonic terrains. In *Drift Exploration in Glaciated Terrane*; McClenaghan, M.B., Bobrowsky, P.T., Hall, G.E.M., Cook, S.J., Eds.; Geological Society of London Special Publications, Burlington House: Picadilly, Londn, UK, 2001; Volume 185, pp. 69–81. [CrossRef]

20. Kelley, K.D.; Eppinger, R.G.; Lang, J.; Smith, S.M.; Fey, D.L. Porphyry copper indicator minerals (PCIMs) in glacial till samples as an exploration tool: Example from the giant Pebble porphyry Cu-Au-Mo deposit. *Geochem. Explor. Environ. Anal.* **2011**, *11*, 321–334. [CrossRef]

21. Celis, M.A.; Bouzari, F.; Bissig, T.; Hart, C.J.R.; Ferbey, T. *Petrographic Characteristics of Porphyry Indicator Minerals from Alkalic Porphyry Copper-Gold Deposits in South-Central British Columbia (NTS 092, 093): Geoscience BC, Summary of Activities 2013*; Report 2014-1; Geoscience BC: Vancouver, BC, Canada; pp. 53–62.

22. Hashmi, S.; Ward, B.C.; Plouffe, A.; Leybourne, M.I.; Ferbey, T. Geochemical and mineralogical dispersal in till from the Mount Polley Cu-Au porphyry deposit, central British Columbia, Canada. *Geochem. Explor. Environ. Anal.* **2015**, *15*, 234–249. [CrossRef]

23. Ricou, L.E.; Burg, J.P.; Godfriaux, I.; Ivanov, Z. Rhodope and Vardari the metamorphic and the olistostromic paired belts related to the Cretaceous subduction under Europe. *Geod. Acta* **1998**, *11*, 285–309. [CrossRef]

24. Mountrakis, D. Tertiary and Quaternary tectonics of Greece. In *Postcollisional Tectonics and Magmatism in the Mediterranean Region and Asia: Geological Society of America Special Paper*; Dilek, Y., Pavlides, S., Eds.; Geological Society of America: Boulder, CO, USA, 2006; Volume 409, pp. 125–136. [CrossRef]

25. Jolivet, L.; Brunn, J.P. Cenozoic geodynamic evolution of the Aegean Region. *Int. J. Earth. Sci.* **2010**, *99*, 109–138. [CrossRef]

26. Ring, U.; Glodny, J.; Will, T.; Thomson, S. The Hellenic subduction system: High pressure metamorphism, exhumation, normal faulting, and large-scale extension. *Ann. Rev. Earth Planet. Sci.* **2010**, *38*, 45–76. [CrossRef]

27. Jolivet, L.; Faccenna, C.; Huet, B.; Labrousse, L.; Le Pourhiet, L.; Lacombe, O.; Lecomte, E.; Burov, E.; Denèle, Y.; Brun, J.-P.; et al. Aegean tectonics: Strain localization, slab tearing and trench retreat. *Tectonophysics* **2013**, *597*, 1–33. [CrossRef]

28. Kydonakis, K.; Brunn, J.-P.; Sokoutis, D. North Aegean core complexes, the gravity spreading of a thrust wedge. *J. Geophys. Res. Solid Earth* **2015**, *120*, 1601. [CrossRef]

29. Kydonakis, K.; Moulas, E.; Chatzitheodoridis, E.; Brunn, J.-P.; Kostopoulos, D. First-report on Mesozoic eclogite-facies metamorphism preceding Barrovian overprint from the western Rhodope (Chalkidiki, northern Greece). *Lithos* **2015**, *220–223*, 147–163. [CrossRef]

30. Voudouris, P.; Tarkian, M.; Arikas, K. Mineralogy of telluride-bearing epithermal ores in Kassiteres-Sappes area, western Thrace, Greece. *Minim. Petrol* **2006**, *87*, 31–52. [CrossRef]

31. Mavrogonatos, C.; Voudouris, P.; Spry, P.G.; Melfos, V.; Klemme, S.; Berndt, J.; Baker, T.; Moritz, R.; Bissig, T.; Monecke, T.; et al. Mineralogical Study of the Advanced Argillic Alteration Zone at the Konos Hill Mo–Cu–Re–Au Porphyry Prospect, NE Greece. *Minerals* **2018**, *8*, 479. [CrossRef]

32. Brun, J.P.; Sokoutis, D. Core complex segmentation in North Aegean, a dynamic view. *Tectonics* **2018**, *37*, 1797–1830. [CrossRef]

33. Turpaud, P.; Reischmann, T. Characterisation of igneous terranes by zircon dating: Implications for UHP occurrences and suture identification in the Central Rhodope, northern Greece. *Int. J. Earth Sci.* **2010**, *99*, 567–591. [CrossRef]

34. Meinhold, G.; Kostopoulos, D.K. The Circum-Rhodope Belt, northern Greece: Age, provenance, and tectonic setting. *Tectonophysics* **2013**, *595–596*, 55–68. [CrossRef]

35. Bonev, N.; Marchev, P.; Moritz, R.; Collings, D. Jurassic subduction zone tectonics of the Rhodope Massif in the Thrace region (NE Greece) as revealed by new U-Pb and ^{40}Ar/^{39}Ar geochronology of the Evros ophiolite and high-grade basement rocks. *Gondwana Res.* **2015**, *27*, 760–775. [CrossRef]

36. Wuthrich, E. Low Temperature Thermochronology of the North Aegean Rhodope Massif. Ph.D. Thesis, Swiss Federal Institute of Technology, Zurich, Switzerland, 2009.

37. Kilias, A.; Falalakis, G.; Sfeikos, A.; Papadimitriou, E.; Vamvaka, A.; Gkarlaouni, C. The Thrace basin in the Rhodope province of NE Greece—A Tertiary supra-detachment basin and its geodynamic implications. *Tectonophysics* **2013**, *595–596*, 90–105. [CrossRef]

38. Del Moro, A.; Innocenti, F.; Kyriakopoulos, C.; Manetti, P.; Papadopoulos, P. Tertiary granitoids from Thrace (Northern Greece): Sr isotopic and petrochemical data. *Neues Jahrb. Mineral. Abh.* **1988**, *159*, 113–115.

39. Marchev, P.; Kaiser-Rohrmeier, B.; Heinrich, C.; Ovtcharova, M.; von Quadt, A.; Raicheva, R. Hydrothermal ore deposits related to post-orogenic extensional magmatism and core complex formation: The Rhodope Massif of Bulgaria and Greece. *Ore Geol. Rev.* **2005**, *27*, 53–89. [CrossRef]

40. Ersoy, E.Y.; Palmer, M.R. Eocene-Quaternary magmatic activity in the Aegean: Implications for mantle metasomatism and magma genesis in an evolving orogeny. *Lithos* **2013**, *180–181*, 5–24. [CrossRef]

41. Pe-Piper, G.; Piper, D.J.W. The igneous Rocks of Greece: The anatomy of an orogen. In *Beiträge der Regionalen Geologie der Erde*; Gebrüder Borntraeger: Berlin, Germany, 2002; p. 573.

42. Moritz, R.; Márton, I.; Ortelli, M.; Marchev, P.; Voudouris, P.; Bonev, N.; Spikings, R.; Cosca, M. A review of age constraints of epithermal precious and base metal deposits of the Tertiary Eastern Rhodopes: Coincidence with Late Eocene-Early Oligocene tectonic plate reorganization along the Tethys. In *XIX Congress of the Carpathian Balkan Geological Association*; Christofides, G., Kantiranis, D., Kostopoulos, D.S., Chatzipetros, A., Eds.; Scientific Annals of the School of Geology A.U.Th. 100: Thessaloniki, Greece, 2010; pp. 351–358.

43. Menant, A.; Jolivet, L.; Vrielynck, B. Kinematic reconstruction and magmatic evolution illuminating crystal and mantle dynamics of the eastern Mediterranean region since the late Cretaceous. *Tectonophysics* **2016**, *675*, 103–140. [CrossRef]

44. Melfos, V.; Voudouris, P. Cenozoic metallogeny of Greece and potential for precious, critical and rare metals exploration. *Ore Geol. Rev.* **2017**, *59*, 1030–1057. [CrossRef]

45. Voudouris, P.; Mavrogonatos, C.; Spry, P.G.; Baker, T.; Melfos, V.; Klemd, R.; Haase, K.; Repstock, A.; Djiba, A.; Bismayer, U.; et al. Porphyry and epithermal deposits in Greece: An overview, new discoveries, and mineralogical constraints on their genesis. *Ore Geol. Rev.* **2019**, *107*, 654–691. [CrossRef]

46. Voudouris, P. Mineralogical, Geochemical and Fluid Inclusion Studies on Epithermal Vein Type Gold/Silver Mineralizations at Kassiteres/Sapes, (NE- Greece). Ph.D. Thesis, University of Hamburg, Hamburg, Germany, 1993.

47. Ortelli, M.; Moritz, R.; Voudouris, P.; Spangenberg, J. Tertiary porphyry and epithermal association of the Sapes-Kassiteres district, Eastern Rhodopes, Greece. In Proceedings of the 10th Biennial SGA Meeting, Townsville, Australia, 17–20 August 2009; pp. 536–538.

48. Voudouris, P. Hydrothermal corundum, topaz, diaspore and alunite supergroup minerals in the advanced argillic alteration lithocap of the Kassiteres-Sapes porphyry-epithermal system, western Thrace, Greece. *Neues Jahrb. Mineral.* **2014**, *191*, 117–136. [CrossRef]

49. Mavrogonatos, C.; Voudouris, P.; Spry, P.G.; Melfos, V.; Klemme, S.; Berndt, J.; Moritz, R.; Kanellopoulos, C. First zunyite-bearing lithocap in Greece: The case of Konos Hill Mo-Re-Cu-Au porphyry system. In Proceedings of the 1st International Electronic Conference on Mineral Science, At sciforum, Basel, Switzerland, 16–31 July 2018; Volume 1. [CrossRef]

50. Voudouris, P.; Melfos, V.; Spry, P.G.; Bindi, L.; Kartal, T.; Arikas, K.; Moritz, R.; Ortelli, M. Rhenium-rich molybdenite and rheniite (ReS$_2$) in the Pagoni Rachi-Kirki Mo-Cu-Te-Ag-Au deposit, Northern Greece. implications for the rhenium geochemistry of porphyry style Cu-Mo and Mo mineralization. *Can. Miner.* **2009**, *47*, 1013–1036. [CrossRef]

51. Voudouris, P.; Melfos, V.; Spry, P.G.; Kartal, T.; Schleicher, H.; Moritz, R.; Ortelli, M. The Pagoni Rachi/Kirki Cu-Mo-Re-Au-Ag-Te deposit, northern Greece: Mineralogical and fluid inclusion constraints on the evolution of a telescoped porphyry-epithermal system. *Can. Miner.* **2013**, *51*, 411–442. [CrossRef]

52. Mavrogonatos, C.; Voudouris, P.; Spry, P.G.; Melfos, V.; Klemme, S.; Berndt, J.; Periferakis, A. Biotite Chemistry from Porphyry-Style Mineralization in Western Thrace, Greece. In Proceedings of the 8th Geochemistry symposium, Antalya, Turkey, 2–6 May 2018; Volume 193.

53. Melfos, V.; Vavelidis, M.; Christofides, G.; Seidel, E. Origin and evolution of the Tertiary Maronia porphyry copper-molybdenum deposit, Thrace, Greece. *Min. Depos.* **2002**, *37*, 648–668. [CrossRef]

54. Galanopoulos, E.; Voudouris, P.; Mavrogonatos, C.; Spry, P.G.; Hart, C.; Melfos, V.; Zaccarini, F.; Alfieris, D.A. New porphyry Mo mineralization at Aisymi-Leptokarya, South-Eastern Rhodope, North-East Greece: Geological and mineralogical constraints. *Geosciences* **2018**, *8*, 435. [CrossRef]

55. Kilias, S.P.; Naden, J.; Paktsevanoglou, M.; Giampouras, M.; Stavropoulou, A.; Apeiranthiti, D.; Mitsis, I.; Koutles, T.; Michael, K.; Christidis, C. Multistage alteration, mineralization and ore–forming fluid properties at the Viper (Sappes) Au–Cu–Ag–Te ore body, W. Thrace, Greece. *Bull. Geol. Soc. Greece* **2013**, *47*, 1635–1644. [CrossRef]

56. Voudouris, P.; Melfos, V.; Spry, P.G.; Moritz, R.; Papavasiliou, C.; Falalakis, G. Mineralogy and geochemical environment of formation of the Perama Hill high sulfidation epithermal Au-Ag-Te-Se deposit, Petrota graben, NE Greece. *Min. Pet.* **2011**, *103*, 79–100. [CrossRef]

57. Dimou, E. A correlative mineralogical study of Achla Tarla and St. Philippos mineralization, Kirki area (NE Greece). *Bull. Geol. Soc. Greece* **1993**, *28*, 37–54. (In Greek)

58. Repstock, A.; Voudouris, P.; Kolitsch, U. New occurrences of watanabeite, colusite, "arsenosulvanite" and Cu-excess tetrahedrite-tennantite at the Pefka high-sulfidation epithermal deposit, northeastern Greece. *N. Jahrb. Min.* **2015**, *192*, 135–149. [CrossRef]

59. Pouchou, J.L.; Pichoir, F. Quantitative analysis of homogeneous or stratified microvolumes applying the model "PAP". In *Electron Probe Quantitation*; Heinrich, K.F.J., Newbury, D.E., Eds.; Plenum Press: New York, NY, USA, 1991; pp. 31–75.

60. Milani, L.; Bolhar, R.; Cawthorn, R.G.; Frei, D. In situ LA-ICP-MS and EPMA trace element characterization of Fe-Ti oxides from the phoscorite-carbonatite association at Phalaborwa, South Africa. *Min. Depos.* **2017**, *52*, 747–768. [CrossRef]

61. van Achterbergh, E.; Ryan, C.G.; Jackson, S.E.; Griffin, W.L. Data reduction software for LA-ICP-MS: Appendix. In *Laser Ablation-ICP Mass Spectrometry in the Earth Sciences: Principles and Applications*; Sylvester, P.J., Ed.; Mineralogical Association Canada (MAC) Short Course Series; MAC: Ottawa, ON, Canada, 2001; Volume 29, pp. 239–243.

62. Griffin, W.L.; Powell, W.J.; Pearson, N.J.; O'Reilly, S.Y. GLITTER: Data reduction software for laser ablation ICP-MS. In *Laser Ablation ICP-MS in the Earth Sciences: Current Practices and Outstanding Issues*; Sylvester, P., Ed.; Short Course Series 40; Mineralogical Association of Canada: Quebec City, QC, Canada, 2008; pp. 308–311.

63. Jochum, K.P.; Weis, U.; Stoll, B.; Kuzmin, D.; Yang, Q.; Raczek, I.; Jacob, D.E.; Stracke, A.; Birbaum, K.; Frick, D.A.; et al. Determinationof reference values for NIST SRM 610–617 glasses following ISO guidelines. *Geostand. Geoanal. Res.* **2011**, *35*, 397–429. [CrossRef]

64. Arikas, K. The porphyry Mo occurrence at Panoni Rachi (NE Kirki) and the mineralogy of hydrothermally altered subvolcanic rocks at Kirki–Esymi area. *Bull. Geol. Soc. Greece* **1991**, *25*, 259–274. (In Greek)

65. Perkins, R.; Copper, F.J.; Condon, D.J.; Tattitsch, B.; Naden, J. Post-collisional Cenozoic extension in the northern Aegean: The high-K to shoshonitic intrusive rocks of the Maronia Magmatic Corridor, northeastern Greece. *Lithosphere* **2018**, *10*, 582–601. [CrossRef]

66. McQueen, K.G.; Cross, A.J. Magnetite as a geochemical sampling medium: Application to skarn deposits. In *The State of the Regolith*; Eggleton, R.A., Ed.; Geological Society of Australia: Brisbane, Australia, 1998; pp. 194–199.

67. Deditius, A.P.; Reich, M.; Simon, A.C.; Suvorova, A.; Knipping, I.; Roberts, M.P.; Rubanov, S.; Dodd, A.; Saunders, M. Nanogeochemistry of hydrothermal magnetite. *Contr. Miner. Pet.* **2018**, *173*. [CrossRef]

68. Frost, B.R.; Lindsley, D.H. Equilibria among Fe-Ti oxides, pyroxenes, olivine, and quartz: Part II. Application. *Am. Miner.* **1992**, *77*, 1004–1020.

69. Toplis, M.J.; Corgne, A. An experimental study of element partitioning between magnetite, clinopyroxene and iron-bearing silicate liquids with particular emphasis on vanadium. *Contrib. Min. Pet.* **2002**, *144*, 22–37. [CrossRef]

70. Sievwright, R.H.; Wilkinson, J.J.; O'Neill, H.S.C.; Berry, A.J. Thermodynamic controls on element partitioning between titanomagnetite and andesitic-dacitic silicate melts. *Contrib. Min. Pet.* **2017**, *172*, 1–33. [CrossRef]

71. Sossi, P.A.; Prytulak, J.; O'Neill, H.S.C. Experimental calibration of vanadium partitioning and stable isotope fractionation between hydrous granitic melt and magnetite at 800 °C and 0.5 GPa. *Contrib. Miner. Pet.* **2018**, *173*, 27. [CrossRef]

72. Sillitoe, R.H. Characteristics and controls of the largest porphyry copper-gold and epithermal gold deposits in the circum-Pacific region. *Aust. J. Earth Sci.* **1997**, *44*, 373–388. [CrossRef]

73. Sinclair, W.D. *Porphyry Deposits*; Special Publication 5; Geological Association of Canada, Mineral Deposits Division: St. John's, NL, Canada, 2007; pp. 223–243.

74. Simon, A.C.; Pettke, T.; Candela, P.A.; Piccoli, P.M.; Heinrich, C.A. Magnetite solubility and iron transport in magmatic-hydrothermal environments. *Geochim. Cosmochim. Acta* **2004**, *68*, 4905–4914. [CrossRef]

75. Oliver, N.H.; Cleverley, J.S.; Mark, G.; Pollard, P.J.; Fu, B.; Marshall, L.J.; Rubenach, M.J.; Williams, P.J.; Baker, T. Modeling the role of sodic alteration in the genesis of iron oxide-copper-gold deposits, Eastern Mount Isa block, Australia. *Econ. Geol.* **2004**, *99*, 1145–1176. [CrossRef]

76. Nadoll, P.; Koenig, A.E. LA-ICP-MS of magnetite: Methods and reference materials. *J. Anal. At. Spectrom.* **2011**, *26*, 1872–1877. [CrossRef]

77. Rudnick, R.L.; Gao, S. Composition of the continental crust. In *Treatise on Geochemistry*; Holland, H.D., Turekian, K.K., Eds.; The Crust Elsevier-Pergamon: Oxford, UK, 2003; Volume 3, pp. 1–64.

78. Ciobanu, C.L.; Cook, N.J. Skarn textures and a case study: The Ocna de Fier-Dognecea orefield, Banat, Romania. *Ore. Geol. Rev.* **2004**, *24*, 315–370. [CrossRef]

79. Einaudi, M.T.; Meinert, L.D.; Newberry, R.J. *Skarn Deposits: 75th Anniversary Volume*; Society of Economic Geologists: Littleton, CO, USA, 1981; pp. 317–391.

80. Meinert, L.D.; Dipple, G.M.; Nicolescu, S. *World Skarn Deposits: Economic Geology 100th Anniversary Volume*; Society of Economic Geologists: Littleton, CO, USA, 2005; pp. 299–336.

81. Pearce, J.A.; Cann, J. Tectonic setting of basic volcanic rocks determined using trace element analyses. *Earth Plan. Sci. Lett.* **1973**, *19*, 290–300. [CrossRef]

82. Floyd, P.A.; Winchester, J.A. Identification and discrimination of altered and metamorphosed volcanic rocks using immobile elements. *Chem. Geol.* **1978**, *21*, 291–306. [CrossRef]

83. Middelburg, J.J.; van der Weijden, C.H.; Woittiez, J.R.W. Chemical processes affecting the mobility of major, minor and trace elements during weathering of granitic rocks. *Chem. Geol.* **1988**, *68*, 253–273. [CrossRef]

84. Hough, R.M.; Noble, R.R.P.; Hitchen, G.J.; Hart, R.; Reddy, S.M.; Saunders, M.; Clode, P.; Vaughan, D.; Lowe, J.; Anand, R.R.; et al. Naturally occurring gold nanoparticles and nanoplates. *Geology* **2008**, *36*, 571–574. [CrossRef]

85. Whalen, J.B.; Anderson, R.G.; Struik, L.C.; Villeneuve, M.E. Gochemistry and Nd isotopes of the François Lake plutonic suite, Endako batholith: Host and progenitor to the Endako molybdenum camp, central British Columbia. *Can. J. Earth Sci.* **2001**, *38*, 603–618. [CrossRef]

86. Yang, X.-M.; Lentz, D.R.; McCutcheon, S.R. Petrochemical evolution of subvolcanic granitoid intrusions within the Late Devonian Mount Pleasant caldera, southwestern New Brunswick, Canada: Comparison of Au versus Sn-W-Mo-polymetallic mineralization systems. *Atl. Geol.* **2003**, *39*, 97–121. [CrossRef]